UC Davis
UC Davis Previously Published Works

Title

Scattering reduction by structured light illumination in line-scanning temporal focusing microscopy.

Permalink

Journal

ISSN

Authors

Xue, Yi
Berry, Kalen P
Boivin, Josiah R
et al.

Publication Date

DOI

Scattering reduction by structured light illumination in line-scanning temporal focusing microscopy

YI XUE,[1,2] **KALEN P. BERRY,**[3] **JOSIAH R. BOIVIN,**[4] **DUSHAN WADDUWAGE,**[2,5] **ELLY NEDIVI,**[3,4,6] **AND PETER T. C. SO**[1,2,5,*]

[1]*Department of Mechanical Engineering, Massachusetts Institute of Technology, 77 Massachusetts Ave., Cambridge, MA 02139, USA*
[2]*Laser Biomedical Research Center, 77 Massachusetts Ave., Cambridge, MA 02139, USA*
[3]*Department of Biology, 77 Massachusetts Ave., Cambridge MA 02139, USA*
[4]*Picower Institute for Learning and Memory,77 Massachusetts Ave., Cambridge, MA 02139, USA*
[5]*Department of Biological Engineering, 77 Massachusetts Ave., Cambridge, MA 02139, USA*
[6]*Department of Brain and Cognitive Sciences, 77 Massachusetts Ave., Cambridge, MA 02139, USA*
[*]*ptso@mit.edu*

Abstract: Line-scanning temporal focusing microscopy (LineTFM) is capable of imaging biological samples more than 10 times faster than two-photon laser point-scanning microscopy (TPLSM), while achieving nearly the same lateral and axial spatial resolution. However, the image contrast taken by LineTFM is lower than that by TPLSM because LineTFM is severely influenced by biological tissue scattering. To reject the scattered photons, we implemented LineTFM using both structured illumination and uniform illumination combined with the HiLo post-processing algorithm, called HiLL microscopy (HiLo-Line-scanning temporal focusing microscopy). HiLL microscopy significantly reduces tissue scattering and improves image contrast. We demonstrate HiLL microscopy with *in vivo* brain imaging. This approach could potentially find applications in monitoring fast dynamic events and in mapping high resolution structures over a large volume.

1. Introduction

Two-photon microscopy is widely used for *in vivo* neurobiological imaging. The use of infrared femtosecond pulses for fluorescence excitation ensures that two-photon microscopy can image much deeper than single photon microscopy with less photodamage. Typical two-photon microscopes are based on a point-scanning approach [1]. Two-photon laser point-scanning microscopy (TPLSM) can produce high contrast images because it uses a point detector, such as a photomultiplier tubes (PMT), to collect all the emitted photons and is insensitive to image blurring due to the scattering of emission photons [2, 3]. However, TPLSM requires sequential scanning and is inherently slow. To achieve faster imaging speed while keeping the same spatial resolution, line-scanning temporal focusing microscopy (LineTFM) has been developed. LineTFM simultaneously focuses light spatially and temporally [4–6]. Briefly, temporal focusing microscopy adds additional dispersion to femtosecond pulses by a grating placed on the conjugate image plane. Therefore, the pulse duration is stretched for locations outside of the image plane. The pulse duration is compressed again only on the image plane. LineTFM temporally focuses light in one direction and spatially focuses light in the other direction. Compared to TPLSM, LineTFM only needs to mechanically scan the object along one direction to image the entire field of view (FOV). Thus, the imaging speed is over 10 times faster than TPLSM.

In *in vivo* imaging, however, scattering reduces image contrast. Images taken by LineTFM suffer more from scattering than images taken by TPLSM due to the fact that LineTFM uses cameras rather than PMTs as detectors. The scattering radius can be tens to hundreds of microns,

which is much larger than the spatial resolution of two-photon microscopy [3]. Thus, the scattered photons are distributed among many pixels of the camera, which reduces the signal of the source and increases the background noise. This problem is particularly severe near bright objects, such as the soma of a neuron; the scattered photons can bury the fluorescence signal from adjacent dendrites and spines. Thus, the image contrast of LineTFM is lower than TPLSM. We propose to overcome this problem using structured illumination (SI).

SI is a common approach today and has been used to increase spatial resolution and obtain axial sectioning capability [7–19]. In the first case, SI increases lateral resolution, even achieving super-resolution [7, 8]. SI encodes sample information, shifting high frequency information, which is originally outside of the numerical aperture, back into the passband. This application of SI requires multiple intermediate images to reconstruct the final image (see Theory) [7]. In the second case, SI can be used to improve the axial sectioning capability of one-photon and two-photon widefield microscopy [9–19]. SI can be modulated on the conjugate image plane [13–15, 19] or the Fourier plane [18]. For example, a digital mirror device (DMD) on the conjugate image plane works as a grating in temporal focusing microscopy while generating SI at the same time [13]. In our previous work, SI is generated by an interference pattern or a Ronchi ruling on the conjugate image plane [14]. There are many SI reconstruction algorithms. The HiLo algorithm is commonly used to provide depth discrimination because it is quite immune to motion artifacts and requires the fewest number of intermediate images [10–12]. HiLo takes two images of the same object with uniform illumination (UI) and structured illumination (SI), respectively. The idea is that the SI image after low-pass filtering retains only in-focus low spatial frequency objects. The UI image after high-pass filtering contains only in-focus high spatial frequency objects. Appropriate merging of information from both images produces the correct depth resolved image on the focal plane.

In this paper, we combined a HiLo algorithm with LineTFM (HiLL) to reduce the scattering effect and increase the contrast of *in vivo* imaging. LineTFM already provides high axial resolution, but the scattered emission photons increase the background and reduce contrast. Therefore, the addition of the HiLo algorithm allows us to selectively reject this diffuse background while retaining the in-focus objects. We first simulated the theoretical spatial resolution of the LineTFM and SI pattern. Then we experimentally measured the point spread function (PSF) of LineTFM, HiLL and line-scanning two-photon microscopy (LineTPM). Next, we performed *in vivo* microscopy in cortical neurons of dual-color fluorescence labeled mice. We compared the images of the same neuron under LineTFM, HiLL and TPLSM. Last, we statistically analyzed the intensity and contrast of *in vivo* images acquired by all three methods. The results indicate that HiLL can significantly reduce the scattering effect and improve the contrast of *in vivo* images, while keeping a high frame rate and high spatial resolution.

2. Theory

2.1. PSF comparison of HiLL and TPLSM

When the back aperture of the objective is overfilled, as it is in our system (see Methods), the axial confinement of LineTFM is the same as that of TPLSM [16]. Thus, it can be described as [16]

$$TPE(z) \approx \frac{1}{1 + (\Delta z / z_R)^2}, \tag{1}$$

where z_R represents the Rayleigh range of the beam and Δz refers to the displacement from the focus. The FWHM of *TPE(z)* defines the axial resolution of LineTFM.

Structured illumination in HiLL can improve axial sectioning and reduce scattering [14]. We calculated the SI intensity change along the z-axis according to the properties of a defocused optical system [20]. With incoherent detection, the optical transfer function (OTF) of the system
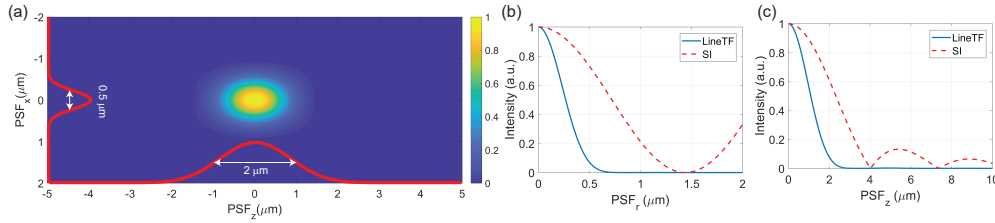
Fig. 1. Simulation results of HiLL. (a) The theoretical PSF of HiLL. (b-c) Comparison of SI pattern and LineTFM PSF in the (b) radial direction and (c) axial direction. The full width of half maximum (FWHM) of the SI pattern is larger than the FWHM of the LineTFM PSF in both directions.

represents the contrast of stripes on the image plane by scanning a thin sheet of fluorescence along the z-axis. We measured the spatial frequency on the image plane $T_g = 2.88\mu m$, which is converted to normalized SI frequency $s = \lambda/(T_g \cdot NA) = 0.378$. The OTF along the z-axis is

$$T_A(z) = A\frac{2J_1\left[k\sin^2(\alpha)s(1 - 0.5s)z\right]}{k\sin^2(\alpha)s(1 - 0.5s)z}. \tag{2}$$

A is the amplitude correction related to SI frequency s, and k is the wave vector. The SI pattern on the focal plane can be described by a sinusoidal function. As shown in Fig. 1, the period of the stripes is larger than the PSF of LineTFM in both the lateral and axial directions. Because LineTFM overfills the back aperture of the objective, the resolution of HiLL equals that of LineTFM in our experiments. For a widefield temporal focusing system, if the axial width of the stripes generated by a higher frequency grid is smaller than the PSF of LineTFM, the axial resolution of HiLL could be further improved, but the contrast of the stripes would be lower [14].

2.2. HiLo algorithm for scattering reduction

Structured illumination is an efficient method to encode spatial information. It is used to increase lateral resolution [7, 21] and reduce out of focus scattering [9–12, 14]. When used in super-resolution microscopy, several intermediate images with SI of different phase shifts are required to reconstruct the final image [7, 9, 21]. For denoising purposes, one UI image and one SI image are required to reconstruct the in focus image by the HiLo algorithm [12]. The key of the HiLo algorithm is that SI only modulates objects that are in focus but not objects that are out of focus. The UI image is [11, 12]

$$U(x) = I_{in}(x) + I_{out}(x), \tag{3}$$

where I_{in} and I_{out} are photons in focus and out of focus, respectively. The images acquired under sinusoidal SI is

$$S(x) = A\left[I_{in}(x)\left(1 + M\cos(k_g x)\right) + I_{out}(x)\right], k_g = 2\pi/T_g. \tag{4}$$

Because I_{out} is not modulated, we can remove I_{out} by subtracting Eq. (4) from Eq. (3), that is,

$$D(x) = \left|U(x) - \frac{S(x)}{A}\right| = I_{in}(x)\left(1 + M\cos(k_g x)\right). \tag{5}$$

This product is a low resolution version of I_{in}. We applied a low-pass (LP) filter to $D(x)$ on the Fourier plane, a Gaussian filter in this case. Different filters can slightly influence the

reconstructed image contrast. The cutoff frequency k_c is smaller than $1/T_g$; normally we choose half of the modulation frequency. So the low-passed image is

$$I_{LP}(x) = \mathcal{F}^{-1}\{\mathcal{F}\{D(x)\} \times LP(k_x)\}. \tag{6}$$

To recover the high resolution part of I_{in}, we applied a high-pass (HP) filter to $U(x)$, because a single structured illumination image lost information smaller than the fringes. The HP filter satisfies $HP(k_x) = 1 - LP(k_x)$. The high-passed image is

$$I_{HP}(x) = \mathcal{F}^{-1}\{\mathcal{F}\{U(x)\} \times HP(k_x)\}. \tag{7}$$

The reconstructed image is a combination of I_{LP} and I_{HP}:

$$I_{HiLo}(x) = \eta I_{LP}(x) + I_{HP}(x), \tag{8}$$

where η adjusts the relative intensity of the two images to combine them seamlessly.

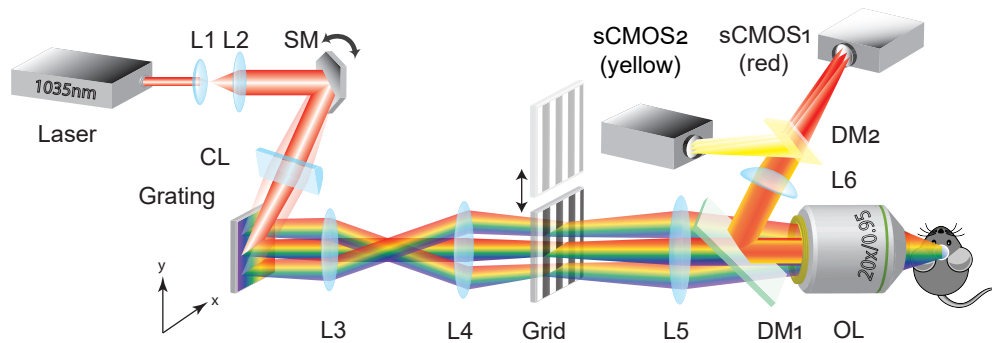## 3. Methods

3.1. The setup of HiLL

Fig. 2. Figure 1. The HiLL setup diagram. Laser: femtosecond laser at a wavelength of 1035nm. L1, L2: relay lenses to collimate the beam. SM: scanning mirror, which scans along the y-axis. CL: cylindrical lens, which focuses the beam in the y-axis. Grating: dispersion along the x-axis. L3, L4: relay lenses. Grid: 10 lp/mm Ronchi ruling to project stripes along the x-axis. L5, L6: tube lenses. DM: dichroic mirror. OL: objective lens (XLUMPlanFL, 20×, 0.95NA, Olympus). The image is detected by sCMOS camera 1 (red channel, Prime95B, Photometrics) and sCMOS camera 2 (yellow channel, PCO edge 5.5, PCO AG).

HiLL is based on the design of a LineTFM [4, 5] with the ability to switch between uniform illumination and structured illumination. The laser generates femtosecond pulses at a wavelength of 1035 nm (repetition rate 1MHz, spectrum width ±5 nm, Monaco, Coherent Inc., CA, USA). The scanning mirror (6350, Cambridge Technology, MA, USA) mechanically scans the beam along the y-axis. The cylindrical lens (f =150 mm) focuses the beam into a line on the grating (20RG1200-1000-2, Newport Co., CA, USA, 1200 grooves/mm). The incident angle θ_i is about 73°, so the 1st order diffraction angle is about 17°. The grating generates dispersion along the x-axis. L3 (f =300 mm) and L4 (f =75 mm) are relay lenses. To generate structured illumination, a Ronchi ruling (38-258, Edmund Optics, NJ, USA) is placed on the conjugate image plane. It is mounted on a magnetic mounting seat so that it can be manually removed when performing uniform illumination. The time to remove the Ronchi ruling is negligible compared to imaging

time (1.6 s per frame). This method is simple, but it is based on the assumption that the sample does not change during the imaging period (about 90 s for one image stack). For faster imaging conditions, we have implemented an SI imaging system with millisecond level switching time between structured and uniform illumination. The contrast of stripes is important for the HiLo process, so we chose 10 line-pair/mm grid that is equivalent to 2.88 μm period on the image plane, which is larger than the PSF of LineTFM. L5 (f =300 mm) is the tube lens. On the back focal plane, the beam size is about 20×20 mm. We overfilled the back aperture so that the spatial resolution of HiLL microscopy is comparable with TPLSM. The FOV is about $250 \times 250 \mu m^2$. L6 (f =350 mm) is the tube lens in the detection path. The system magnification is about 40× according to the objective magnification and the focal length of tube lenses. The image is detected by two sCMOS cameras simultaneously, working as a red channel and yellow channel (separated by dichroic mirror 2, FF560-FDi02-t3-25x36, Semrock, NY, USA), respectively (see Appendix for detailed design calculations).

3.2. *Experimental parameters for TPLSM and HiLL imaging*

To visualize weak fluorescent structures, such as dendrites and spines, the imaging average power and exposure time [22–26] are selected to achieve sufficient signal-to-noise ratio from weak fluorescent structures inside the mouse brain, and to remain below the power threshold of two-photon excitation saturation [27]. The parameters used in the following calculation come from experimental conditions we have optimized for imaging the dendrites of L2/3 pyramidal neurons *in vivo* [22–26]. We compared the imaging speed of HiLL with TPLSM under conditions yielding the same number of emission photons. The number of emission photons within a diffraction limited spot is related to pulse energy and the number of pulses in the exposure time. Thus, we imaged the same neuron with both systems and adjusted the power and acquisition time to equalize the pulse energy and pulse number (Fig. 4-5 and Fig.6-7).

The laser source of TPLSM is a Ti:Sapphire femtosecond laser. The average power out of the objective is about 40 mW, the repetition rate is 80MHz, and the dwell time of each pixel is 40 μs. The dwell time is longer than in many other imaging studies, because the small structures we image are relatively dim and are in some cases located at depths of more than 100 μm from the surface of the brain. The maximum pulse energy for most fluorescent proteins is about $40mW/80MHz = 0.5nJ$ without fluorescence saturation while the number of pulses is $40\mu s \times 80MHz = 3200$ and the size of diffraction limited spots is about 500 nm. Thus, to fulfill the constraints of the Nyquist theorem, the step size is 250 nm/pixel. A $250 \times 250 \mu m^2$ FOV requires about 1000×1000 pixels (500×500 spots) so the imaging time of one frame is $40\mu s \times 1000 \times 1000 = 40s$.

The radial resolution of LineTFM is about 0.5 μm, and the FOV is about $250 \times 250 \mu m^2$. The sampling rate of each diffraction limited spot is 3 pixels, with a pixel size of 0.16 μm. Thus, LineTFM parallelizes $N = 250/0.5 = 500$ diffraction limited spots in a single line. The pulse energy per line is $0.5nJ \times 500 = 250nJ$. The repetition rate of the laser is 1MHz, so the average power per line is $p_0 = 250nJ \times 1MHz = 250mW$. To receive an equal number of pulses compared to TPLSM, the dwell time of a single line is $3200/1MHz = 3.2ms$. The scanning direction also has 500 diffraction limited spots, so the frame exposure time is $3.2ms \times 500 = 1.6s$. HiLL requires one stack with uniform illumination and another stack with structured illumination, so the total imaging time of HiLL is 3.2 s per frame. Compared to the frame rate of TPLSM, HiLL is about $40/3.2 = 12.5$ times faster.

3.3. *Animal procedures*

In utero electroporation on embryonic day (E)15.5-timed pregnant C57BL/6J mice was performed to label L2/3 cortical pyramidal neurons, as previously described [28]. Animals were coelectroporated with Cre-dependent constructs expressing mScarlet-I and Venus-gephyrin under

the Ubiquitin C promoter, along with a plasmid expressing Cre recombinase at a ratio of 10:5:1, respectively (total DNA concentration 2 μg/μL), with 0.1% Fast Green for visualization. A total of 0.75 μl of the plasmid solution was injected into the right lateral ventricle with a 32G Hamilton syringe (Hamilton Company). Five pulses of 36 V (duration 50 ms, frequency 1 Hz) targeting the visual cortex were delivered from a square-wave electroporator (ECM830; Harvard Apparatus) using 5 mm diameter platinum electrodes (Protech International). After in utero electroporation, pups were raised to adulthood and implanted with a 5 mm cranial window over the right hemisphere as described previously [26] to provide optical access. Imaging was performed under isoflurane anesthesia.

4. Results
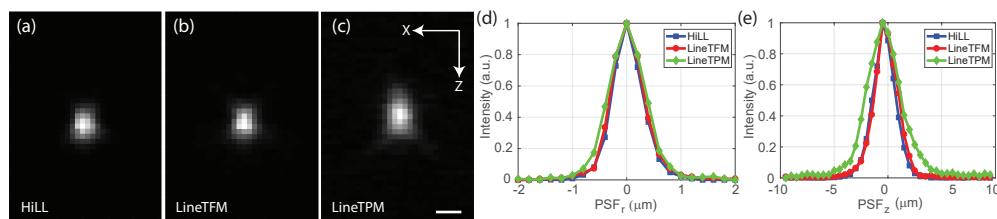
4.1. PSF measurement of LineTFM and HiLL

Fig. 3. (a) The experimental PSF of HiLL; (b) The experimental PSF of LineTFM; (c) The experimental PSF of line-scanning two photon microscopy (LineTPM). (d-e) The PSF of HiLL (blue), PSF of LineTFM (red) and PSF of LineTPM (green) in the (d) radial direction and (e) axial direction.

We measured the PSF of HiLL, LineTFM and line-scanning two photon microscopy (LineTPM) respectively using 200 nm red fluorescent beads (Carboxylate-modified Microspheres, red fluorescent (580/605), ThermoFisher Scientific, MA, USA) (Fig. 3). The PSF of HiLL was calculated according to Eq. (6-8) after acquiring image stacks of these beads under UI LineTFM and SI LineTFM, respectively. The radial resolution is about 0.63 μm and the axial resolution is about 2.28 μm. The PSF is almost the same with and without HiLo processing. Both HiLL and LineTFM (FWHMr=0.67 μm, FWHMz=2.42 μm) have a smaller PSF than LineTPM (FWHMr=0.77 μm, FWHMz=3.48 μm), because temporal focusing overfills the back aperture rather than only a line on the back focal plane in LineTPM. The experimental results are consistent with the theoretical calculation above (Fig. 2) and previous work [15].

4.2. In vivo imaging

We imaged mice expressing mScarlet-I as a cell fill to label dendritic morphology and Venus-gephyrin to labeled inhibitory synapses. We imaged the same neurons using LineTFM, HiLL and TPLSM. The comparison of the same cell imaged by these three methods is shown in Fig. 4. Here, TPLSM works as a ground truth to evaluate HiLL microscopy. For *in vivo* imaging, bright objects contribute more to the scattered photons than do dim objects. The scattered photons add to background intensity, which lowers the contrast of the images (Fig. 4a). The HiLo algorithm has a more obvious effect on contiguously labeled objects (Fig. 4-5, mScarlet-I cell fill) than on sparsely distributed ones (Fig. 4-5, Venus puncta). Comparing Fig. 4 (a1) and (b1), HiLL efficiently removes the scattered photons from the soma and bright dendrites without depleting fine structures such as spines. In other words, weak fluorescent structures are more visible, which are blurry in the homogeneously illuminated image. However, Venus-gephyrin labeled inhibitory synapses are nearly identical in HiLL and LineTFM. Unlike the mScarlet-I cell fill, inhibitory
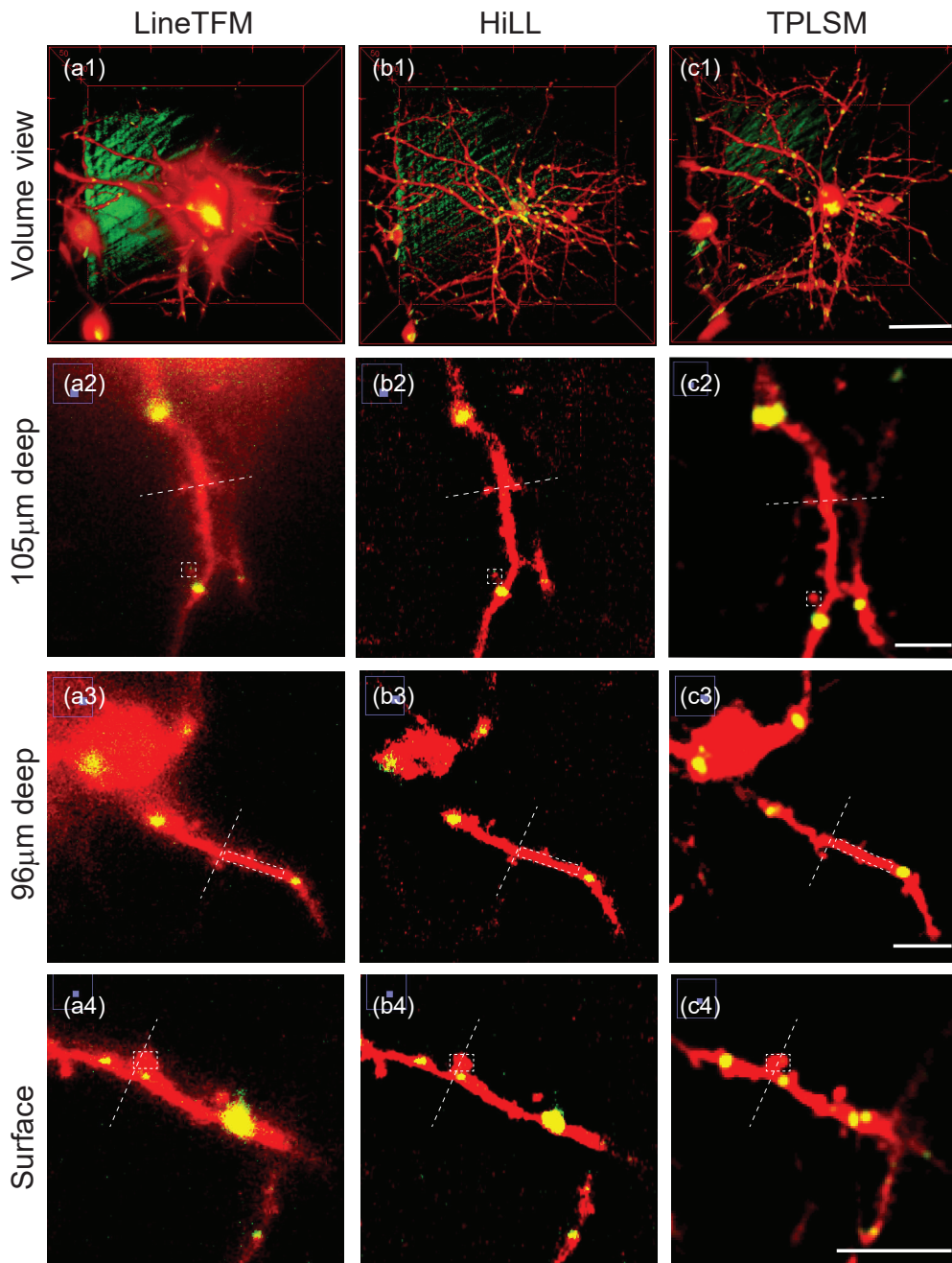
Fig. 4. Imaging the same neuron in a mouse brain in vivo by (a) LineTFM, (b) HiLL and (c) TPLSM. (a1, b1, c1) Volume view of the whole neuron. Scale bar, 50 μm. (a2, b2, c2) Zoomed in on one dendrite at a depth of 105 μm. (a3, b3, c3) Zoomed in on one dendrite at a depth of 96 μm. (a4, b4, c4) Zoomed in on one dendrite near the surface. Red, cell fill by mScarlet. Yellow, Venus-gephyrin at inhibitory synapses. Scale bar, 10 μm.

synapses distribute sparsely, and the size of each synapse is small. Thus, the scattered photons in the Venus-gephyrin channel contribute comparably less background fluorescence; the scattered photons rarely cover adjacent labels. HiLL has less influence on image contrast for sparsely distributed objects. In addition, we imaged dendritic branches at different depths. Fig. 4 shows the magnified images of the results, from 100 μm deep (Fig. 4 (a2-c2), (a3-c3)) to the surface (Fig. 4(a4-c4)). The photons originally deep inside the tissue suffer from scattering; thus the contrast is lower for deeper structures than for superficial structures. HiLL has a more obvious effect on structures deep inside tissue than on superficial structures.
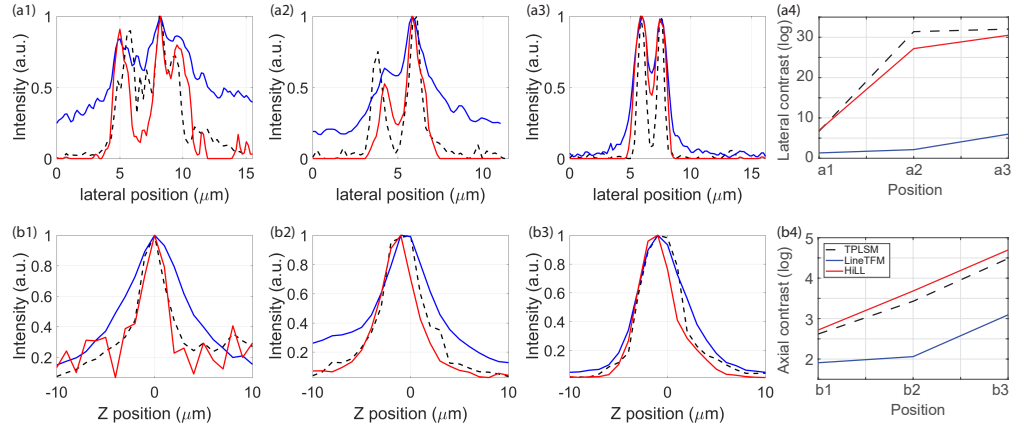

Fig. 5. Quantitative comparison among LineTFM, HiLL and TPLSM in the lateral and axial directions. (a1-a3) Normalized intensity profiles in the lateral direction. The intensity profiles are corresponding to the white dash lines in Fig. 4. (a4) Lateral contrast calculated from (a1-a3). Y-axis is in log scale, (b1-b3) Normalized intensity profiles in the axial direction. The intensity profiles are corresponding to the white dash boxes in Fig. 4. (b4) Axial contrast calculated from (b1-b3). Y-axis is in log scale. (a1, b1) Intensity profiles of Fig. 4a2, b2, c2. (a2, b2) Intensity profiles of Fig. 4a3, b3, c3. (a3, b3) Intensity profiles of Fig. 4a4, b4, c4.

We further quantitatively analyzed the image stack in Fig. 4 to specifically evaluate contrast. Fig. 5 shows the normalized intensity profiles of the regions marked by white dashed lines in Fig. 4. HiLL reduces the scattering effect in both the lateral and axial directions. As a consequence, small objects are more distinguishable in HiLL than LineTFM, nearly the same as TPLSM. For example, Fig. 5a shows the intensity profile across dendrites and spines. HiLL and TPLSM can identify the spines clearly, while LineTFM cannot. In addition, the effect of reducing scattering is more obvious in deep tissue (Fig. 5(a1-2), (b1-2)) than on the surface (Fig. 5(a3), (b3)), because photon scattering is more severe in deep tissue. The contrast improvement of HiLL is shown in Fig. 5(a4) and Fig. 5(b4). The contrast is calculated according to $C = I_{max}/I_{min}$, where I_{max} is the maximum intensity in the intensity profile, and I_{min} is the minimum non-zero intensity in the intensity profile. Because I_{min} is very small in HiLL and TPLSM, C is plotted in log scale. HiLL has similar contrast with TPLSM in both the lateral and axial directions. We also show another dataset in the Appendix, which has the same conclusion as this one. In summary, HiLL significantly improves contrast compared to LineTFM, especially near soma and bright dendrites.

5. Summary

We demonstrate that HiLL microscopy combining the HiLo algorithm with line-scanning temporal focusing microscopy can improve image contrast while maintaining high imaging speed and spatial resolution. Our results show that the system is applicable for *in vivo* imaging of mouse

brain at a 3 s frame rate covering a FOV over 250 μm. This approach can be applied to monitoring rapid structural changes of objects such as synapses in the intact brain, or for monitoring the movement or structural dynamics of other objects in scattering tissues.

6. Appendix

6.1. Theoretical calculation

The lenses and gratings are selected to achieve a sufficiently large FOV and overfill the back aperture at the same time. L1 and L2 are to collimate beam and expand it to the size of x_0. After that, along the x-axis, the beam is collimated until the grating adds dispersion to it. The incident angle to the grating is θ_i. Along the y-axis, the beam is focused by a cylindrical lens, and the grating is on the focal plane of the cylindrical lens. We used matrix methods to calculate the beam size at back aperture and FOV.

After grating, the input beam is $[x_{in}, \alpha_{in}]'$, where $x_{in} = x_0/\cos\theta_i$, $\alpha_{in} = \frac{\Delta\lambda}{d\cos\theta}$. $\Delta\lambda$ is the spectrum width of laser, which is 10 nm here. d is the groove spacing of the grating, which is 1/1200 mm. θ is the diffraction angle of the grating, which is related to the incident angle by $\sin\theta_i + \sin\theta = m\lambda/d$, where m=1 for the 1st order diffraction.

Then the lens matrix is $\begin{bmatrix} 1 & 0 \\ -1/f_j & 1 \end{bmatrix}$, and the propagation matrix is $\begin{bmatrix} 1 & f_j \\ 0 & 1 \end{bmatrix}$, $j = 3, 4, 5$. In our setup, $f_3 = 300$mm, $f_4 = 75$mm, $f_5 = 300$mm. Thus, the size of beam along x-axis on the back aperture is:

$$\begin{bmatrix} x_{BA} \\ \alpha_{BA} \end{bmatrix} = \begin{bmatrix} 1 & f_5 \\ 0 & 1 \end{bmatrix} \begin{bmatrix} 1 & 0 \\ -1/f_5 & 1 \end{bmatrix} \begin{bmatrix} 1 & f_4 + f_5 \\ 0 & 1 \end{bmatrix} \begin{bmatrix} 1 & 0 \\ -1/f_4 & 1 \end{bmatrix} \begin{bmatrix} 1 & f_3 + f_4 \\ 0 & 1 \end{bmatrix} \begin{bmatrix} 1 & 0 \\ -1/f_3 & 1 \end{bmatrix} \begin{bmatrix} 1 & f_3 \\ 0 & 1 \end{bmatrix} \begin{bmatrix} x_{in} \\ \alpha_{in} \end{bmatrix}. \tag{9}$$

$x_{BA} \approx 20$mm. For y-axis,

$$y_{BA} = \frac{f_3}{f_{CL}} \cdot \frac{f_5}{f_4} \cdot y_{in}. \tag{10}$$

To match with x-direction beam size, we chose the focal length of the cylindrical lens to be 150 mm, then y_{BA} is about 20 mm on the back aperture. Both directions overfill the back aperture. The objective is 20 ×, 0.95NA from Olympus, so the FOV is:

$$\begin{bmatrix} x_{FOV} \\ \alpha_{FOV} \end{bmatrix} = \begin{bmatrix} 1 & f_{OL} \\ 0 & 1 \end{bmatrix} \begin{bmatrix} 1 & 0 \\ -1/f_{OL} & 1 \end{bmatrix} \begin{bmatrix} 1 & f_{OL} \\ 0 & 1 \end{bmatrix} \begin{bmatrix} x_{BA} \\ \alpha_{BA} \end{bmatrix}, \tag{11}$$

which is about 250 μm. y_{FOV} can be easily adjusted by changing the voltage on scan mirror. We choose the focal length of L6 to be 350 mm according to the pixel size of cameras to fulfill Nyquist Theorem.
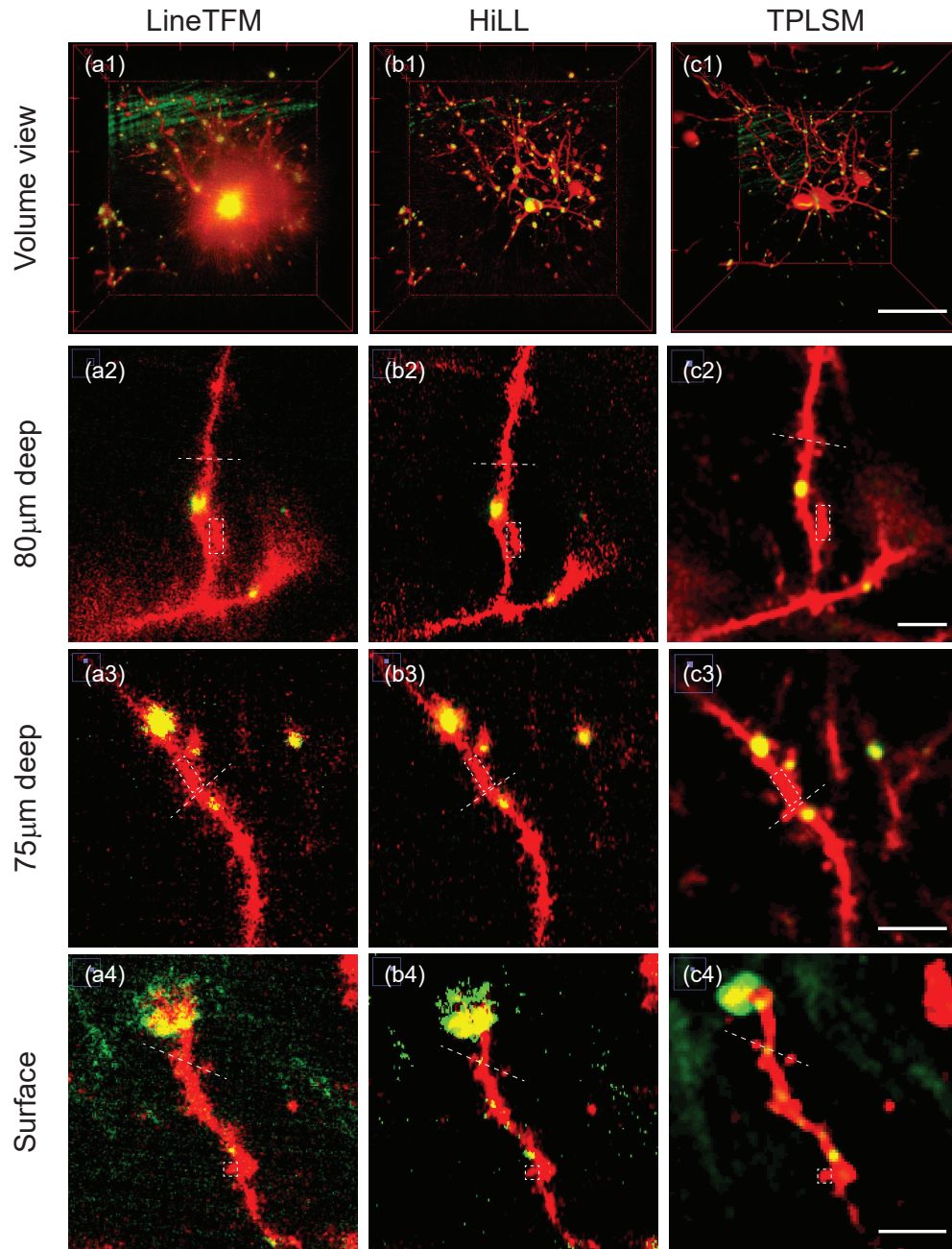
6.2. Experimental results

Fig. 6. Imaging the same neuron of mouse brain in vivo by (a) LineTFM, (b) HiLL and (c) TPLSM. (a1, b1, c1) Volume view of the whole neuron. Scale bar, 50 μm. (a2, b2, c2) Zoomed in on one dendrite in the depth of 85 μm. (a3, b3, c3) Zoomed in on one dendrite at a depth of 80 μm. (a4, b4, c4) Zoomed in on one dendrite near surface. Red, cell fill by Scarlet. Yellow, Venus-gephyrin at inhibitory synapses. Scale bar, 10 μm.
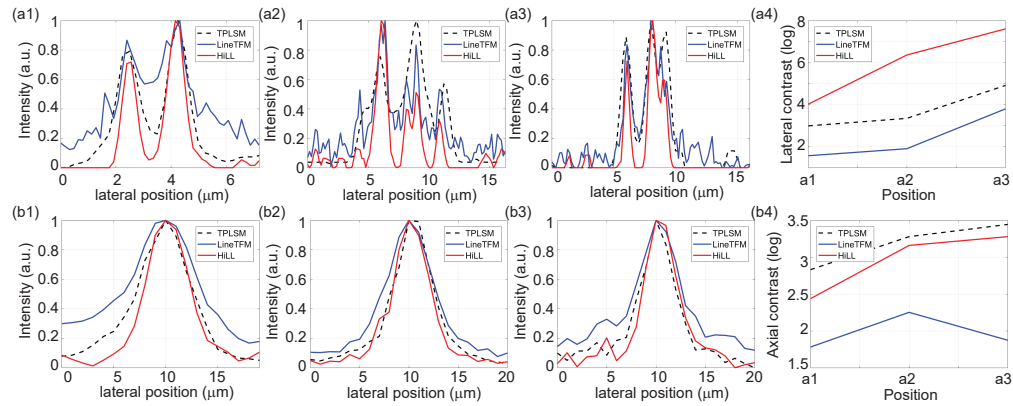
Fig. 7. Quantitative comparison among LineTFM, HiLL and TPLSM in the lateral and axial directions. (a1-a3) Normalized intensity profiles in the lateral direction. The intensity profiles are corresponding to the white dash lines in Fig. 6. (a4) Lateral contrast calculated from (a1-a3). Y-axis is in log scale, (b1-b3) Normalized intensity profiles in the axial direction. The intensity profiles are corresponding to the white dash boxes in Fig. 6. (b4) Axial contrast calculated from (b1-b3). Y-axis is in log scale. (a1, b1) Intensity profiles of Fig. s1 a2, b2, c2. (a2, b2) Intensity profiles of Fig. s1 a3, b3, c3. (a3, b3) Intensity profiles of Fig. s1 a4, b4, c4.

Disclosure

The authors declare that there are no conflicts of interest related to this article.

References

1. W. Denk, J. H. Strickler, and W. W. Webb, "Two-photon laser scanning fluorescence microscopy," Science **248**, 73–76 (1990).
2. F. Helmchen and W. Denk, "Deep tissue two-photon microscopy," Nat. Methods **2**, 932–940 (2005).
3. K. H. Kim, C. Buehler, K. Bahlmann, T. Ragan, W.-C. A. Lee, E. Nedivi, E. L. Heffer, S. Fantini, and P. T. C. So, "Multifocal multiphoton microscopy based on multianode photomultiplier tubes," Opt. Express **15**, 11658–11678 (2007).
4. E. Tal, D. Oron, and Y. Silberberg, "Improved depth resolution in video-rate line-scanning multiphoton microscopy using temporal focusing," Opt. Lett. **30**, 1686–1688 (2005).
5. G. Zhu, J. van Howe, M. Durst, W. Zipfel, and C. Xu, "Simultaneous spatial and temporal focusing of femtosecond pulses," Opt. Express **13**, 2153–2159 (2005).
6. H. Dana and S. Shoham, "Remotely scanned multiphoton temporal focusing by axial grism scanning," Opt. Lett. **37**, 2913–2915 (2012).
7. M. G. Gustafsson, "Surpassing the lateral resolution limit by a factor of two using structured illumination microscopy," J. Microsc. **198**, 82–87 (2000).
8. T. A. Planchon, L. Gao, D. E. Milkie, M. W. Davidson, J. A. Galbraith, C. G. Galbraith, and E. Betzig, "Rapid three-dimensional isotropic imaging of living cells using bessel beam plane illumination," Nat. Methods **8**, 417–423 (2011).
9. M. A. Neil, R. Juskaitis, and T. Wilson, "Method of obtaining optical sectioning by using structured light in a conventional microscope," Opt. Lett. **22**, 1905–1907 (1997).
10. J. Mertz, "Optical sectioning microscopy with planar or structured illumination," Nat. Methods **8**, 811–819 (2011).
11. J. Mertz and J. Kim, "Scanning light-sheet microscopy in the whole mouse brain with HiLo background rejection," J. Biomed. Opt. **15**, 016027 (2010).
12. D. Lim, K. K. Chu, and J. Mertz, "Wide-field fluorescence sectioning with hybrid speckle and uniform-illumination microscopy," Opt. Lett. **33**, 1819–1821 (2008).
13. L.-C. Cheng, C.-H. Lien, Y. Da Sie, Y. Y. Hu, C.-Y. Lin, F.-C. Chien, C. Xu, C. Y. Dong, and S.-J. Chen, "Nonlinear structured-illumination enhanced temporal focusing multiphoton excitation microscopy with a digital micromirror device," Biomed. Opt. Express **5**, 2526–2536 (2014).
14. H. Choi, E. Y. S. Yew, B. Hallacoglu, S. Fantini, C. J. R. Sheppard, and P. T. C. So, "Improvement of axial resolution and contrast in temporally focused widefield two-photon microscopy with structured light illumination," Biomed. Opt. Express **4**, 995–1005 (2013).
15. E. Y. S. Yew, C. J. R. Sheppard, and P. T. C. So, "Temporally focused wide-field two-photon microscopy: paraxial to vectorial," Opt. Express **21**, 12951–12963 (2013).
16. M. E. Durst, G. Zhu, and C. Xu, "Simultaneous spatial and temporal focusing in nonlinear microscopy," Opt. Commun. **281**, 1796–1805 (2008).
17. P. Rupprecht, R. Prevedel, F. Groessl, W. E. Haubensak, and A. Vaziri, "Optimizing and extending light-sculpting microscopy for fast functional imaging in neuroscience," Biomed. Opt. Express **6**, 353–368 (2015).
18. Y. Zhang, L. Kong, H. Xie, X. Han, and Q. Dai, "Enhancing axial resolution and background rejection in line-scanning temporal focusing microscopy by focal modulation," Opt. Express **26**, 21518–21526 (2018).
19. Z. Li, J. Hou, J. Suo, C. Qiao, L. Kong, and Q. Dai, "Contrast and resolution enhanced optical sectioning in scattering tissue using line-scanning two-photon structured illumination microscopy," Opt. Express **25**, 32010–32020 (2017).
20. P. A. Stokseth, "Properties of a defocused optical system*," J. Opt. Soc. Am., JOSA **59**, 1314–1321 (1969).
21. M. G. L. Gustafsson, L. Shao, P. M. Carlton, C. J. R. Wang, I. N. Golubovskaya, W. Z. Cande, D. A. Agard, and J. W. Sedat, "Three-dimensional resolution doubling in wide-field fluorescence microscopy by structured illumination," Biophys. J. **94**, 4957–4970 (2008).
22. K. L. Villa, K. P. Berry, J. Subramanian, J. W. Cha, W. C. Oh, H.-B. Kwon, Y. Kubota, P. T. C. So, and E. Nedivi, "Inhibitory synapses are repeatedly assembled and removed at persistent sites in vivo," Neuron **89**, 756–769 (2016).
23. J. L. Chen, K. L. Villa, J. W. Cha, P. T. C. So, Y. Kubota, and E. Nedivi, "Clustered dynamics of inhibitory synapses and dendritic spines in the adult neocortex," Neuron **74**, 361–373 (2012).

24. J. L. Chen, W. C. Lin, J. W. Cha, P. T. So, Y. Kubota, and E. Nedivi, "Structural basis for the role of inhibition in facilitating adult brain plasticity," Nat. Neurosci. **14**, 587–594 (2011).

25. W.-C. A. Lee, J. L. Chen, H. Huang, J. H. Leslie, Y. Amitai, P. T. So, and E. Nedivi, "A dynamic zone defines interneuron remodeling in the adult neocortex," Proc. Natl. Acad. Sci. pp. nas–0810149105 (2008).

26. W.-C. A. Lee, H. Huang, G. Feng, J. R. Sanes, E. N. Brown, P. T. So, and E. Nedivi, "Dynamic remodeling of dendritic arbors in GABAergic interneurons of adult visual cortex," PLoS Biol. **4**, e29 (2006).

27. G. C. Cianci, J. Wu, and K. M. Berland, "Saturation modified point spread functions in two-photon microscopy," Microsc. Res. Tech. **64**, 135–141 (2004).

28. H. Tabata and K. Nakajima, "Efficient in utero gene transfer system to the developing mouse brain using electroporation: visualization of neuronal migration in the developing cortex," Neuroscience **103**, 865–872 (2001).